Defect induced, layer-modulated magnetism in ultrathin metallic PtSe$_2$

Ahmet Avsar[1,2,*], **Alberto Ciarrocchi**[1,2], **Michele Pizzochero**[3], **Dmitrii Unuchek**[1,2], **Oleg V. Yazyev**[3], **Andras Kis**[1,2,*]

[1]Electrical Engineering Institute, École Polytechnique Fédérale de Lausanne (EPFL), Lausanne CH 1015, Switzerland [2]Institute of Materials Science and Engineering, École Polytechnique Fédérale de Lausanne (EPFL), Lausanne CH 1015, Switzerland [3]Institute of Physics, École Polytechnique Fédérale de Lausanne (EPFL), Lausanne CH 1015, Switzerland

Abstract

Defects are ubiquitous in solids, often introducing new properties that are absent in pristine materials. One of the opportunities offered by these crystal imperfections is an extrinsically induced long-range magnetic ordering,1 a long-time subject of theoretical investigations.1–3 Intrinsic, two-dimensional (2D) magnetic materials4–7 are attracting increasing attention for their unique properties including layer-dependent magnetism4 and electric field modulation6. Yet, inducing magnetism into otherwise non-magnetic 2D materials remains a challenge. Here, we investigate magneto-transport properties of ultrathin PtSe$_2$ crystals and demonstrate unexpected magnetism. Our electrical measurements show the existence of either ferromagnetic or anti-ferromagnetic ground state orderings depending on the number of layers in this ultra-thin material. The change in the device resistance upon application of a ~ 25 mT magnetic field is as high as 400 Ω with a magnetoresistance (MR) value of 5%. Our first-principles calculations suggest that surface magnetism induced by the presence of Pt vacancies and the Ruderman-Kittel-Kasuya-Yosida (RKKY) exchange couplings across ultra-thin films of PtSe$_2$ are responsible for the observed layer-dependent magnetism. Considering the existence of such unavoidable growth-related vacancies in 2D materials, 8,9 these findings can expand the range of 2D ferromagnets into materials that would otherwise be overlooked.

While intrinsically magnetic materials are rare in nature, long-range magnetism can be introduced into non-magnetic 2D materials through adatom intercalation,[10] proximity coupling,[11] and defect engineering[12] thanks to their large surface area to volume ratios. The latter strategy has been predicted for several 2D metallic materials including graphene,[2] but this has not been experimentally realized yet. Recently, $PtSe_2$ has been considered to be an ideal platform for investigating defect-induced magnetization.[13,14] First-principles calculations show that Se and especially Pt vacancies in monolayer $PtSe_2$ have a strong influence on its electronic properties; a large magnetic moment of up to 6 μ_B is expected for single or double Pt vacancies. Such defects in 2D materials can either form naturally during the growth/annealing processes[8] or they can be intentionally created post-synthesis, e.g., under electron beam irradiation.[15] Point defects including Pt vacancies are present at the topmost layers in chemical vapor transport-grown $PtSe_2$.[9] Considering the existence of these unavoidable point defects in as-grown material[9] and its metallic behavior above a critical thickness,[16,17] $PtSe_2$ holds a great promise for spintronic applications.

We obtain thin, ribbon-shaped $PtSe_2$ flakes by mechanical exfoliation from chemical vapor transport -grown bulk crystals (HQ Graphene) onto a Si/SiO_2 (270 nm) substrate. In total, ten devices were characterized with $PtSe_2$ thickness varying between ~ 4.15 nm to ~ 14 nm, as determined by atomic force microscopy (AFM), allowing us to study the thickness dependence of the magnetism. *Non-magnetic* metallic Palladium (Pd) contacts (80 nm thick) were formed using electron beam lithography and electron beam evaporation techniques. These non-magnetic Pd contacts were fabricated to exclude any influence of the contact on the magnetic response of the device. Due to the ribbon-like shape of our crystals, devices were fabricated in the two-terminal geometry. An AFM image of a completed device is shown in Figure 1a. Longitudinal device resistance was characterized as a function of back-gate voltage (V_{BG}), source-drain bias (V_{SD}), magnetic field and temperature.

We first discuss the charge transport properties of a device based on a 5.2 nm thick $PtSe_2$ crystal (device A). Figure 1b shows the gate-voltage (V_{BG}) dependence of source-drain current I_{SD} at fixed bias-voltage (V_{SD}) values of 50, 100 and 200 mV where we observe nearly gate-independent transport characteristics. This indicates that 5.2 nm $PtSe_2$ is metallic, in good agreement with recent findings. This is also confirmed by the observation of *nearly* linear I_{SD}-V_{SD} relation even at low temperatures (Figure 1c) and by studying the temperature dependence of the device resistance (Supplementary Information 1). Since semiconducting behavior was observed in thinner samples (it is also challenging to electrically probe magnetism in such resistive samples (Supplementary Information 2-3)), we focus on crystals thicker than 4.15 nm for the remainder of this manuscript.

We utilize magnetoresistance measurements as a sensing tool to characterize the magnetism in $PtSe_2$. For this, we sweep an out-of-plane magnetic field (B) while recording the device resistance. As shown in Figure 2a, we observe a hysteresis loop with minima at ± 25 mT under backward and forward scans. Such hysteretic behavior and the presence of a minor loop (Supplementary Information 4) are the hallmarks of ferromagnetism and were previously observed in ferromagnetic metals such as Cobalt (Co) under the same measurement geometry.[18] We extract a coercive field of ~ 25 mT which is also comparable to the one observed in Co wires.[18] We observe a similar magnetoresistance response in five

different samples with comparable coercive field values (Supplementary Information 5). We also note that, just like the total device resistance, the change in the device resistance under a magnetic field is almost insensitive to the V_{BG} (Supplementary Information 6).

Next, we study the dependence of the change of device resistance (R) on the bias voltage and the temperature. Figure 2b shows the V_{SD} dependence of R measured at 1.6 K. The signal increases from R = 30 Ω to 400 Ω as the bias is reduced from 50 mV to 1 mV. The extracted MR percental variation is 5% at low biases (Supplementary Information 7). As shown in Figure 2b, dependencies of both R and device resistance on V_{SD} are similar and could be due to slightly non-linear charge injection at low biases. Its physical origin needs further investigation. Following, we present the temperature dependence of the magnetoresistance measured at a fixed bias of V_{SD} = 5 mV (Figure 2c). R has a very weak temperature dependence in the 1.5 K < T < 13 K range. Raising the temperature just slightly over 13 K quickly suppresses the magnetic response of the device. The temperature dependence of device resistance also shows a similar sudden drop when T is raised above 13 K, which could be related to the suppression of spin-dependent scattering. The resistance keeps increasing as the temperature is further increased, due to the metallic nature of $PtSe_2$ (Supplementary Information 1).

In contrast to this hysteretic magneto-transport response, another subset containing five out of ten characterized devices shows different characteristics (Supplementary Information 8-9). In Figure 3a, we show the magnetic field dependence (forward and backward sweep directions) of the device resistance for one of these devices (device B), which exhibits plateaus with two different values. Here, we observe the lower plateau at low fields in the -30 mT < B < 30 mT range, whereas a sharp jump to the high plateau is observed for fields above |30| mT. The height of the jump in this device is R ~ 2 Ω and depends on the V_{SD}, as shown in Figure 3b. The width and height of this plateau are also strongly sensitive to the temperature, as the signal completely disappears above 5 K (Figure 3c). Here, we are confident that the transition between these plateaus is a result of the switching between antiferromagnetic ordering at low fields into a fully spin polarized state at higher fields due to the metamagnetic effect.[19] Such magneto-transport response with two plateaus was previously observed in semiconducting bilayer CrI_3-based tunneling devices.[20,21] It was shown that each CrI_3 layer has initially opposite spin polarization at low fields and that the application of a field above the coercive field reverses the magnetization of one of CrI_3 layers causing both layers to have the same spin polarization. Additionally, the observation of very sharp switching between low and high plateaus indicates the out-of-plane direction magneto-crystalline anisotropy of $PtSe_2$, in good agreement with recent predictions.[14] If the anisotropy had in-plane components, the switching would occur gradually with the field.

After presenting the existence of both ferromagnetic and antiferromagnetic ordering in metallic $PtSe_2$, we next check if there is a layer dependent magnetization. The natural way to investigate this dependence would be to compare magneto-transport response of mono and bilayer $PtSe_2$. $PtSe_2$ is however extremely resistive in this thickness range.[16] Instead, we have characterized two adjacent devices prepared under identical conditions. As confirmed by the AFM scan, thickness of $PtSe_2$ crystals in these devices differs by only one layer, as shown in Figure 4a-b, which allows us to investigate layer-dependent magnetism. While the

device with a 6.45 nm thick (10-11 layers-device C) $PtSe_2$ shows the characteristic response with two plateaus (Figure 4c), the device with an extra layer (device D) shows ferromagnetic response (Figure 4d). This observation indicates the layer-dependent magnetism in $PtSe_2$. To further investigate this effect, we prepared another $PtSe_2$ device (device E) containing additional one-layer thick fragments on the channel surface, as revealed by AFM imaging (Figure 4e). Magneto-transport response of this sample is very intriguing: both ferromagnetic and antiferromagnetic ordering coexist (Figure 4f). This measurement also allows us to directly conclude that the switching fields for these two contrasting magnetic orderings are different. Here, the strong layer-dependent relationship between different mechanisms could be stabilizing magnetic ordering differently and hence results in different switching fields. This observation is in good agreement with the different coercive fields probed by magneto-optic Kerr effect (MOKE) measurements for even and odd layers of insulating CrI_3 magnets.[4] Existence of either ferromagnetic or antiferromagnetic ground state orderings depending on the number of layers is intriguing.

In the following, we propose a theoretical picture to interpret the observed effects. As pristine $PtSe_2$ does not present any intrinsic spin-polarization, neither in bulk nor in multilayer form, we suggest that the observed magnetism originates from lattice imperfections (Supplementary Information 10). The appropriate model describing the interaction between magnetic impurities mediated by conduction electrons is the well-established RKKY model.[22–24] According to this, the dependence of magnetic exchange coupling J on the distance R reads as $J(R) \approx cos(2k_FR)/R^\alpha$, with k_F being the Fermi wavevector of the metal hosting the magnetic impurities. The Fermi surface of $PtSe_2$ is composed of closed electron and hole pockets located at $k_z = 0$ and electron pockets at $k_z = \pm 0.6 \, \pi/c$.[25,26] The latter give rise to an oscillating and power-law decaying contribution to $J(R)$ in the direction normal to the $PtSe_2$ layers with a period of approximately two layers, as schematically shown in Figure 5a. Hence, we see that adding or removing *one* layer from metallic $PtSe_2$ is sufficient to change the sign of the magnetic exchange coupling, thereby realizing a thickness-dependent ferro- or anti-ferromagnetic configuration. This observation is also in a good agreement with the summary of devices measured at fixed bias of $V_{SD} = 50$ mV and 100 mV. As shown in Fig. 5a-inset and Supplementary Information 12, we observe that MR decreases as crystal thickness increases, layer-dependent magnetism exist and magnetism is not detectable in thicker crystals.

Next, we step from model interactions to first-principles calculations performed on realistic models in order to suggest which type of defects may be responsible for the magnetic response observed in our samples. Earlier experimental investigations revealed the abundance of vacancy point defects in $PtSe_2$ films.[9] Motivated by this, we assess the impact of such defects on the magnetic properties of $PtSe_2$ by introducing Se (V_{Se}) and Pt (V_{Pt}) vacancy in both metallic multilayer and bulk $PtSe_2$ models. In analogy with other transition metal dichalcogenides,[27] we find that the V_{Se} defect does not lead to magnetism (Supplementary Information 10). On the other hand, the introduction of the V_{Pt} defect at the surface of the multilayer model induces a local magnetic moment of ~1.2 μ_B per defect. We further observe that the spin density around the V_{Pt} defect mostly localizes on the neighboring selenium atoms within its first coordination shell, as shown in Figure 5b. Additionally, the investigation of the electronic density of states reported in Figure 5c

indicates that the local magnetic moments stem from defect-induced spin-split states that emerge around the Fermi level. Remarkably, we find that the same defect does not lead to a local magnetic moment when forming in the bulk (Supplementary Information 10,12). Similarly, extrinsic adsorbents do not induce magnetism (Supplementary Information 11). It is worth noting in this context that $PtSe_2$ is more prone to hosting metal atom vacancies than conventional, group VI dichalcogenides (e.g. MoS_2) as a consequence of the substantially lower formation energy that this defect exhibits in the former material9 as compared to the latter.27

In contrast to recently discovered intrinsic ferromagnets,4–6 $PtSe_2$ has some key advantages for immediate research: it is stable in its pristine form (Supplementary Information 13) without the need for an encapsulation process,17 it can be easily grown with various scalable methods,28 and readily isolated from its as-prepared substrate which makes it transferrable onto any arbitrary substrate.28 Compared to these intrinsic metallic ferromagnets, the currently observed critical temperature in $PtSe_2$ is small. This could be in principle improved by control of the vacancy concentration (to increase the concentration and total magnitude of the resulting magnetic moment), control of crystal thickness (to control the sign of the coupling and the switching fields as discussed above) and Fermi level energy (to modulate the density of states at the Fermi level) in future experiments.

Contrary to the assumption that defects in 2D materials are detrimental for the overall crystal quality, defect engineering could be a key approach to enriching their functionality by inducing magnetism in air-stable materials. In the case of $PtSe_2$, combining the defect-induced magnetism with unique thickness-dependent properties could have several applications for realizing spintronic devices using atomically thin materials.29–31 Thin semiconducting $PtSe_2$ could be utilized as a magnetic substrate for proximity studies.32,33 On the other hand, thick metallic $PtSe_2$ could be integrated into lateral and vertical spin torque devices,34 tunneling magneto-resistance devices,35 and spin valve devices36 for generating spin polarized charge carriers.

Methods

Device fabrication

$PtSe_2$ crystals were obtained by mechanical exfoliation from bulk crystals (HQ Graphene) onto a doped Si substrate with 270 nm of SiO_2. The substrate was imaged by using a color camera equipped optical microscope (Olympus BX51M). The thickness of selected crystals was determined by using AFM topography imaging (Asylum Research Cypher). Metallic contacts were prepared using e-beam lithography (Raith EBPG 5000+, 100 keV thermal field emission gun with a beam does of ~ 950 $\mu C/cm^2$) and e-beam evaporation of Pd (Alliance-Concept EVA 760, 80 nm thick), without the use of any adhesion layers such as Cr or Ti.

Measurements

Cryogenic measurements were performed in an ICE Oxford liquid helium continuous flow cryo-magnetic system with a base temperature of ~ 1.5 K. Drain currents were measured

using a Keithley Sourcemeter 2450, while a Keithley Sourcemeter 2400 was used for applying bias through the SiO_2 gate dielectric. The drain voltage was varying between 1 mV to 1 V, while the source was grounded. Electronic transport measurements were carried out in a two-terminal configuration.

First-principles calculations

First-principles calculations have been performed within the generalized gradient approximation to density functional theory devised by Perdew, Burke and Ernzerhof.[37] Geometry optimizations have been carried out with the VASP code,[38,39] using a kinetic energy cutoff of 400 eV and k-meshes equivalent to 18 k-points per unit cell along each periodic direction. During geometry optimizations, lattice constants and interlayer spacing were constrained to their experimental values of 3.73 Å and 5.08 Å, respectively, while the tolerance on atomic forces was set to 0.02 eV/Å. The electronic density of states has been calculated with the SIESTA code,[40] using a fine mesh equivalent to 120 k-points and a smearing of 0.02 eV. The adopted multilayer and bulk $PtSe_2$ models consist of a a 6-layer thick 3×3 supercell and a periodic $3 \times 3 \times 2$ supercell, respectively. In the case of multilayer models, the defects are placed in the topmost layer and a vacuum region of 15 Å was introduced to separate periodic images.

Supplementary Material

Refer to Web version on PubMed Central for supplementary material.

Acknowledgements

References

1. Esquinazi P, Hergert W, Spemann D, Setzer A, Ernst A. Defect-induced magnetism in solids. IEEE Trans Magn. 2013; 49:4668–4674.

2. Yazyev OV, Helm L. Defect-induced magnetism in graphene. Phys Rev B. 2007; 75

3. Osorio-Guillén J, Lany S, Barabash SV, Zunger A. Magnetism without magnetic ions: percolation, exchange, and formation energies of magnetism-promoting intrinsic defects in CaO. Phys Rev Lett. 2006; 96

4. Huang B, et al. Layer-dependent ferromagnetism in a van der Waals crystal down to the monolayer limit. Nature. 2017; 546:270–273. [PubMed: 28593970]

5. Gong C, et al. Discovery of intrinsic ferromagnetism in two-dimensional van der Waals crystals. Nature. 2017; 546:265–269. [PubMed: 28445468]

6. Deng Y, et al. Gate-tunable room-temperature ferromagnetism in two-dimensional Fe_3GeTe_2. Nature. 2018; 563:94–99. [PubMed: 30349002]

7. Bonilla M, et al. Strong room-temperature ferromagnetism in VSe_2 monolayers on van der Waals substrates. Nat Nanotechnol. 2018; 13:289–293. [PubMed: 29459653]

8. Zhou W, et al. Intrinsic structural defects in monolayer molybdenum disulfide. Nano Lett. 2013; 13:2615–2622. [PubMed: 23659662]

9. Zheng H, et al. Intrinsic point defects in ultrathin 1T-PtSe$_2$ layers. arXiv:1808.04719 [cond-mat]. 2018

10. Hardy WJ, et al. Very large magnetoresistance in Fe$_{0.28}$TaS$_2$ single crystals. Phys Rev B. 2015; 91

11. Wang Z, Tang C, Sachs R, Barlas Y, Shi J. Proximity-induced ferromagnetism in graphene revealed by the anomalous Hall effect. Phys Rev Lett. 2015; 114

12. Guguchia Z, et al. Magnetism in semiconducting molybdenum dichalcogenides. Sci Adv. 2018; 4

13. Gao J, et al. Structure, stability, and kinetics of vacancy defects in monolayer PtSe$_2$: A first-principles study. ACS Omega. 2017; 2:8640–8648. [PubMed: 31457396]

14. Zhang W, et al. Magnetism and magnetocrystalline anisotropy in single-layer PtSe$_2$: Interplay between strain and vacancy. J Appl Phys. 2016; 120

15. Krasheninnikov AV, Nordlund K. Ion and electron irradiation-induced effects in nanostructured materials. J Appl Phys. 2010; 107

16. Ciarrocchi A, Avsar A, Ovchinnikov D, Kis A. Thickness-modulated metal-to-semiconductor transformation in a transition metal dichalcogenide. Nat Commun. 2018; 9:919. [PubMed: 29500434]

17. Zhao Y, et al. High-electron-mobility and air-stable 2D layered PtSe$_2$ FETs. Adv Mater. 2017; 29

18. Leven B, Dumpich G. Resistance behavior and magnetization reversal analysis of individual Co nanowires. Phys Rev B. 2005; 71

19. Huang F, Kief MT, Mankey GJ, Willis RF. Magnetism in the few-monolayers limit: A surface magneto-optic Kerr-effect study of the magnetic behavior of ultrathin films of Co, Ni, and Co-Ni alloys on Cu(100) and Cu(111). Phys Rev B. 1994; 49:3962–3971.

20. Song T, et al. Giant tunneling magnetoresistance in spin-filter van der Waals heterostructures. Science. 2018; 360:1214–1218. [PubMed: 29724908]

21. Klein DR, et al. Probing magnetism in 2D van der Waals crystalline insulators via electron tunneling. Science. 2018; 360:1218–1222. [PubMed: 29724904]

22. Ruderman MA, Kittel C. Indirect exchange coupling of nuclear magnetic moments by conduction electrons. Phys Rev. 1954; 96:99–102.

23. Kasuya T. A Theory of metallic ferro- and antiferromagnetism on Zener's model. Prog Theor Phys. 1956; 16:45–57.

24. Yosida K. Magnetic properties of Cu-Mn alloys. Phys Rev. 1957; 106:893–898.

25. Zhang K, et al. Experimental evidence for type-II Dirac semimetal in PtSe$_2$. Phys Rev B. 2017; 96

26. Clark OJ, et al. Dual quantum confinement and anisotropic spin splitting in the multivalley semimetal PtSe$_2$. Phys Rev B. 2019; 99

27. Pizzochero M, Yazyev OV. Point defects in the 1T' and 2H phases of single-layer MoS$_2$: A comparative first-principles study. Phys Rev B. 2017; 96

28. Yu X, et al. Atomically thin noble metal dichalcogenide: a broadband mid-infrared semiconductor. Nat Commun. 2018; 9:1545. [PubMed: 29670119]

29. Žutić I, Fabian J, Das Sarma S. Spintronics: Fundamentals and applications. Rev Mod Phys. 2004; 76:323–410.

30. Han W, Kawakami RK, Gmitra M, Fabian J. Graphene spintronics. Nat Nanotechnol. 2014; 9:794–807. [PubMed: 25286274]

31. Wen H, et al. Experimental demonstration of xor operation in graphene magnetologic gates at room temperature. Phys Rev Applied. 2016; 5

32. Žutić I, Matos-Abiague A, Scharf B, Dery H, Belashchenko K. Proximitized materials. Materials Today. 2019; 22:85–107.

33. Scharf B, Xu G, Matos-Abiague A, Žutić I. Magnetic Proximity effects in transition-metal dichalcogenides: Converting excitons. Phys Rev Lett. 2017; 119

34. Yang T, Kimura T, Otani Y. Giant spin-accumulation signal and pure spin-current-induced reversible magnetization switching. Nat Phys. 2008; 4:851–854.

35. Moodera JS, Kinder LR, Wong TM, Meservey R. Large Magnetoresistance at room temperature in ferromagnetic thin film tunnel junctions. Phys Rev Lett. 1995; 74:3273–3276. [PubMed: 10058155]

36. Avsar A, et al. Gate-tunable black phosphorus spin valve with nanosecond spin lifetimes. Nat Phys. 2017; 13:888–893.

37. Perdew JP, Burke K, Ernzerhof M. Generalized gradient approximation made simple. Phys Rev Lett. 1996; 77:3865–3868. [PubMed: 10062328]

38. Kresse G, Furthmüller J. Efficient iterative schemes for ab initio total-energy calculations using a plane-wave basis set. Phys Rev B. 1996; 54:11169–11186.

39. Kresse G, Joubert D. From ultrasoft pseudopotentials to the projector augmented-wave method. Phys Rev B. 1999; 59:1758–1775.

40. Soler JM, et al. The SIESTA method for ab initio order- N materials simulation. J Phys: Condens Matter. 2002; 14:2745.
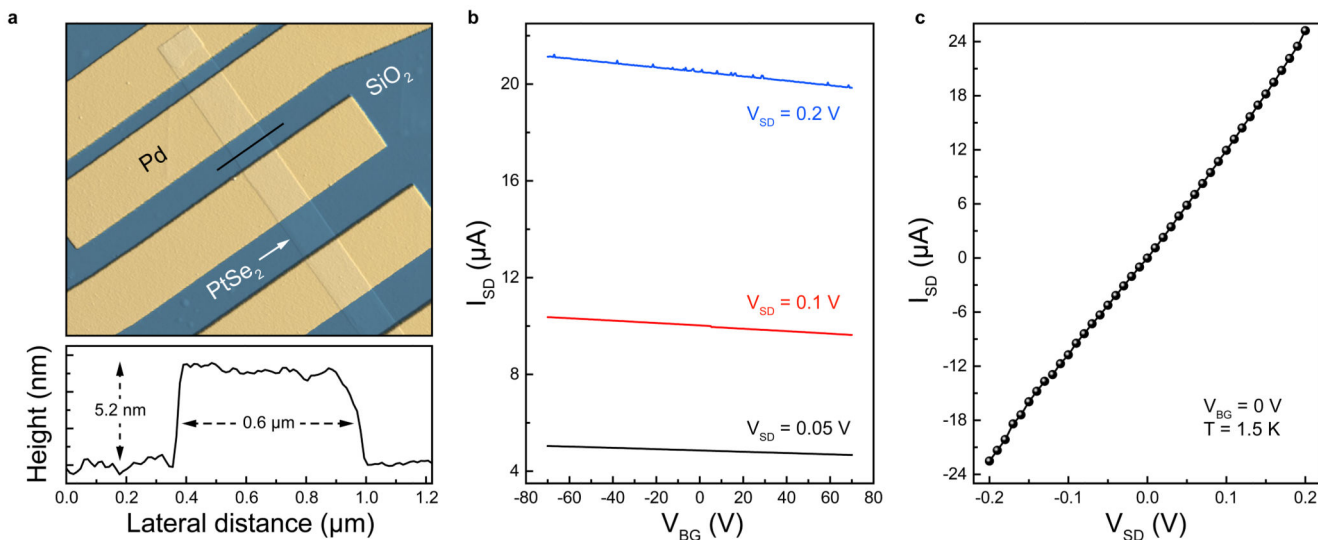
Figure 1. Device structure and basic characterization.
a, An AFM image of the device A. Height scale bar is ± 40 nm. Following the black dashed line, we measure a height of 5.2 nm and a width of 0.6 μm for this device. **b,** V_{BG} dependence of I_{SD} measured at fixed V_{SD} = 0.05 V, 0.1 V and 0.2 V. **c,** Output characteristics of the device as a function of V_{SD} at fixed V_{BG} = 0 V. All charge transport measurements were performed at 1.5 K.
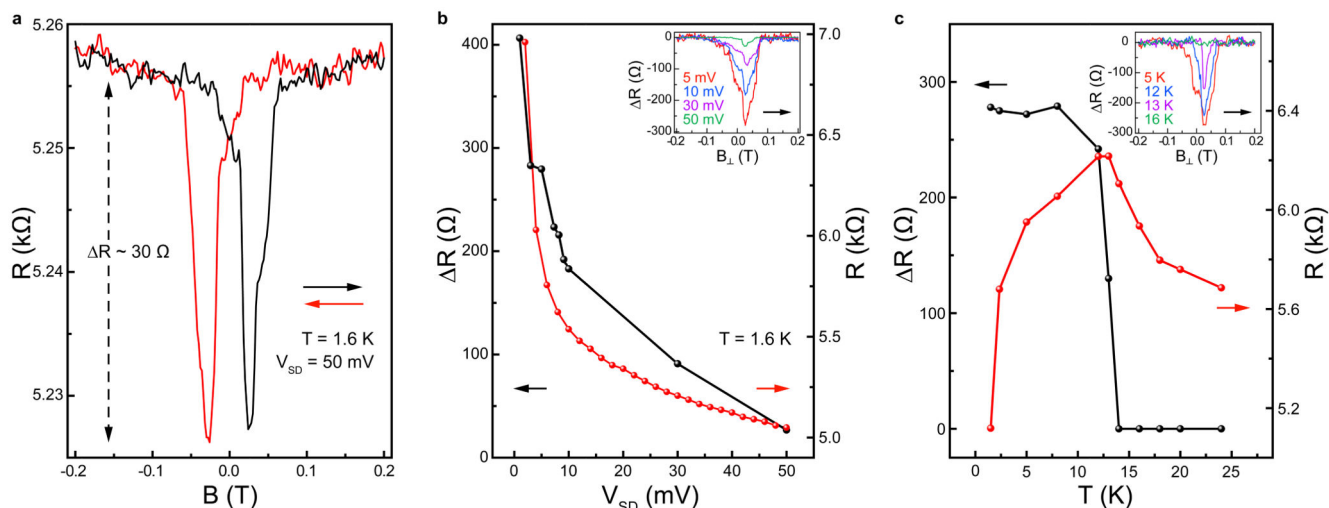
Figure 2. Bias and temperature dependent magnetoresistance measurements in device A.
a, Magnetic field dependence of the device resistance measured at T = 1.6 K. The red (black) arrow represents sweep direction from 0.2 T (-0.2 T) to –0.2 T (0.2 T). **b,** Source-drain bias (V_{SD}) dependences of the change in the device resistance under the magnetic field (ΔR) and the longitudinal device resistance (R). Inset shows the resistance change under magnetic field acquired at fixed biases of V_{SD} = 1 mV, 3 mV and 50 mV. ΔR is calculated by subtracting a polynomial fitting from the device resistance (Supplementary Information 15). **c,** Temperature dependence of ΔR and R. Inset shows the magnetic field dependence of the resistance change measured at T = 1.5 K, 13 K and 16 K.
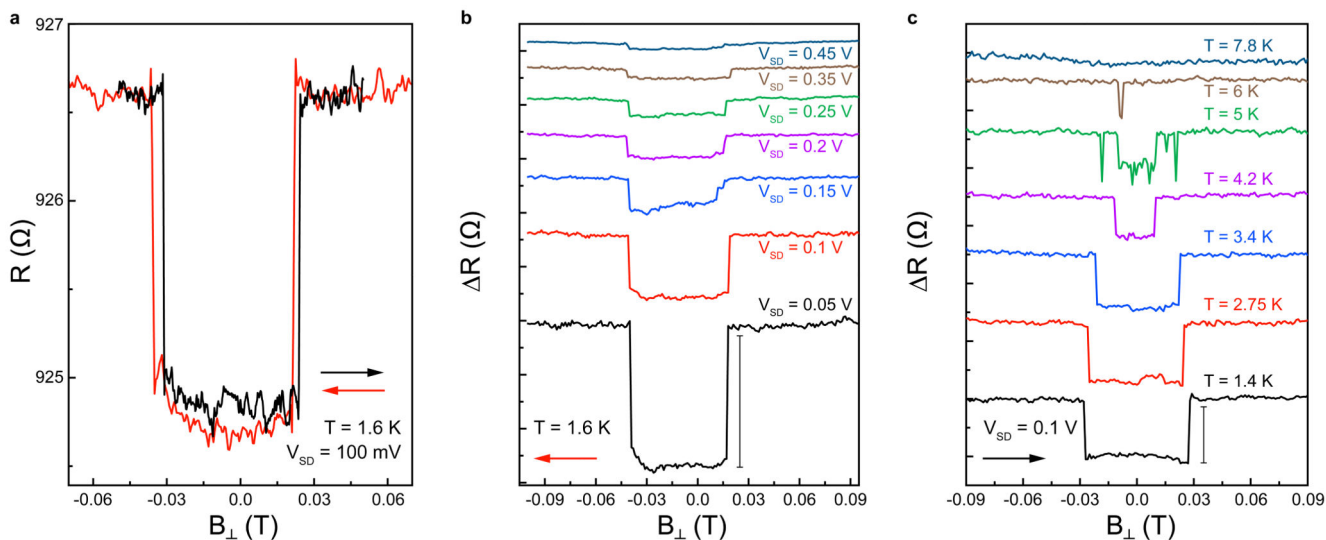
Figure 3. Bias and temperature dependent magnetoresistance measurements in device B (~ 9 nm thick).

a, Magnetic field dependence of the device resistance. The red (black) arrow represents the sweep direction from positive (negative) to negative (positive) values. **b,** V_{SD} dependence of the magneto-resistance change measured at T = 1.5 K. Scale bar is 5 Ω. Curves shown for sweeps at 0.1 V ≤ V_{SD} ≤ 0.45 V are offset for clarity. **c,** Temperature dependence of ΔR measured at fixed bias of V_{SD} = 0.1 V. Scale bar is 2 Ω. Curves shown for sweeps at 2.75 K ≤ T ≤ 7.8 K are offset for clarity.
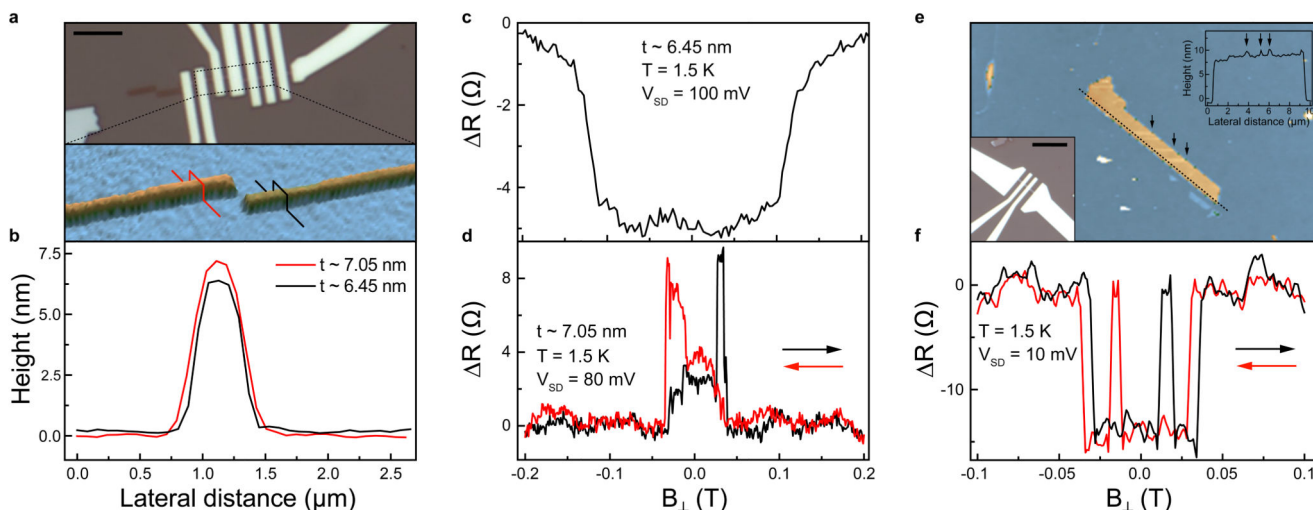
Figure 4. Layer-dependent magnetoresistance measurements.
a, Optical and AFM images of a completed PtSe$_2$ device and its crystal, respectively. Dashed area represents the scanned AFM region. **b.** Cross-sectional plots along the red and black lines in **a.** AFM scans show that crystals used in device C and device D has one-layer difference (~ 0.6 nm) in their heights. **c,** Magnetic field dependence of R measured from the device C (6.45 nm thick). **d,** Magnetic field dependence of R measured from device D (~ 7.05 nm thick). **e,** AFM image of a PtSe$_2$ crystal having multiple one-layer thick fragments on its surface. Top inset shows the cross-sectional plots along the black line in **e.** Black color arrows in **e** and **top-inset e** indicate the one-layer thick fragments. **Bottom-inset e** shows the optical image of the corresponding device. Black solid line represents the scale bar (5 μm) **f,** Magnetic field dependence of R measured from the device E shown in **e**. We would like to note that the change in device resistance in these samples has opposite sign compared to the thinner devices shown in Fig. 2-a and Fig. S4-a. Such opposite switching signs were previously observed in Co and CoFe films.35 To determine the origin of this behavior, the effect of the number of layers, distribution of defects and their effect on magnetism need to be extensively investigated.
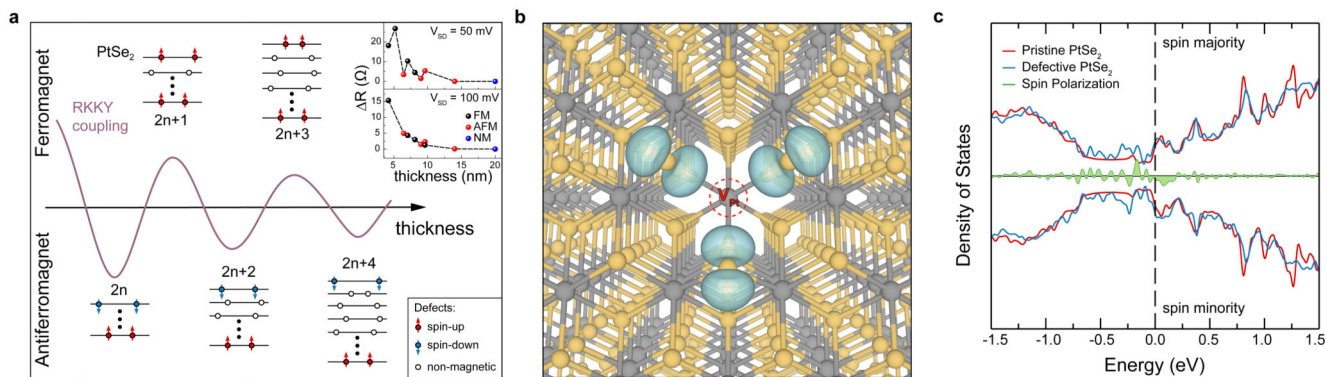
Figure 5. Theoretical investigations of PtSe$_2$.

a, Schematic illustration showing the oscillating RKKY interaction across the PtSe$_2$ slab and the corresponding ground-state magnetic configurations. Inset plot shows the thickness dependence of MR curves for studied samples at fixed V$_{SD}$ of 50 mV and 100 mV. **b,** Atomic structure and spin density (turquoise) around a surface V$_{Pt}$ defect (red, dotted circle) in multilayer PtSe$_2$. Grey (orange) balls represent Pt (Se) atoms. Isosurfaces contour is set to 0.003 e Å^{-3}. **c,** Electronic density of states of multilayer PtSe$_2$ with (blue) and without (red) a surface Pt vacancy defect. In green, the difference between spin majority and spin minority states. Fermi level is set to zero (vertical dashed line).